materials

Article

Shear Behaviour and Calculation Methods of Bearing-Shear Connectors for Prefabricated Steel–Concrete Composite Beams

Zhichao Zheng [1], Yang Zou [2], Yaling Chou [3], Fengjiang Qin [1,*], Fengmin Chen [4], Jin Di [1] and Zhigang Zhang [1]

[1] Key Laboratory of New Technology for Construction of Cities in Mountain Area, School of Civil Engineering, Chongqing University, Chongqing 400030, China; zhichaozheng1@163.com (Z.Z.); dijin@cqu.edu.cn (J.D.); zhangzg@cqu.edu.cn (Z.Z.)
[2] State Key Laboratory of Mountain Bridge and Tunnel Engineering, Chongqing Jiaotong University, Chongqing 400074, China; zouyang@cqjtu.edu.cn
[3] Key Laboratory of Disaster Prevention and Mitigation in Civil Engineering, Lanzhou University of Technology, Lanzhou 730050, China; chouyaling@lzb.ac.cn
[4] China Railway Changjiang Transport Design Group Co., Ltd., Chongqing 401121, China; chenfengmin@ccrdi.cmhk.com
* Correspondence: qinfengjiang@cqu.edu.cn

Abstract: The bearing-shear connector (B-SC) is a newly developed connector that exhibits excellent shear behaviour and is easy to process. However, research on the application of B-SCs as substitutes for grouped studs in prefabricated steel–concrete composite beams is rare, and systematically studying their shear behaviour is necessary. Thus, a refined numerical model was developed to study the shear behaviour of the B-SCs. The numerical model, validated by push-out tests, was conducted to analyse the stress of the B-SCs and concrete slab during loading and to explore the failure mechanism of B-SCs. Then, a parametric study was performed to identify the key factors influencing the shear behaviour of the B-SCs. The concrete strength, and the thickness and the tensile strength of the shear plate were found to significantly influence the shear behaviour of B-SCs. According to the experiments and numerical analysis, calculation formulae for the ultimate shear resistance and slip modulus were proposed.

Keywords: bearing-shear connectors; numerical analysis; failure mechanism; shear resistance; slip modulus; calculation formulae

Citation: Zheng, Z.; Zou, Y.; Chou, Y.; Qin, F.; Chen, F.; Di, J.; Zhang, Z. Shear Behaviour and Calculation Methods of Bearing-Shear Connectors for Prefabricated Steel–Concrete Composite Beams. *Materials* **2023**, *16*, 4616. https://doi.org/10.3390/ma16134616

Academic Editor: Giovanni Garcea

Received: 24 May 2023
Revised: 16 June 2023
Accepted: 19 June 2023
Published: 26 June 2023

1. Introduction

Prefabricated steel–concrete composite bridges have been increasingly used in many countries owing to their advantages, such as good economy, simple construction, and convenient disassembly and replacement in the later stages [1–4]. The main components, concrete decks and steel beams, are prefabricated in the factory and then transported to the site for assembly, which dramatically shortens the construction period and minimises traffic interference. The mechanical performance of prefabricated composite structures is significantly affected by the behaviour of shear connectors [5].

Common shear connectors suitable for prefabricated composite bridges include studs, bolts, and section-steel connectors. Studs are the most common choice for prefabricated composite bridges. However, grouped studs were required to be compactly arranged in bridges with large shear force at the S-C (steel beam–concrete slab) interface, which would increase the size of the reserved holes in precast concrete decks [6–8] that not only increase the difficulty of formwork but also cause the reinforcing bars and grouped studs to interfere with each other in the reserved holes. In response to the above-mentioned problems, multiple studies [9–12] suggest using large-diameter studs. Push-out tests have demonstrated that the application of large-diameter studs improves the shear resistance per stud but also increases the risk of concrete slab splitting [12]. Compared with studs, bolts are not only more convenient to install and disassemble but also have better fatigue strength because they do not require welding [13]. The shear resistance of bolts is close to that of studs of the same size, but their slip modulus is inferior to that of studs [13–16]. Channel connectors [17–20] and C-connectors [21–23] have the advantages of easy processing, small reserved holes, and high shear resistance. However, their initial slip modulus is lower and they have different mechanical properties in opposite directions [20]. Additionally, owing to the existence of a steel flange, concrete is prone to cracking during loading. T-perfobond connectors have the advantages of high shear resistance and slip modulus [24]. However, the failure of T-perfobond connectors is often accompanied by the brittle crushing failure of concrete. The plastic deformation of T-perfobond connectors cannot be large enough to redistribute the load in actual structures owing to their poor deformation ability.

The bearing-shear connectors (B-SCs), composed of pressure-bearing plates and shear plates, have a simple structural design, as illustrated in Figure 1 [25]. Push-out and beam tests are often performed to investigate the shear behaviour of connectors. However, studying the shear behaviour of connectors through a large number of full-scale tests is difficult because of time and cost. Finite element (FE) modelling, as an effective alternative, has been used by many researchers to investigate the shear behaviour of connectors [26–30]. Therefore, this study aims at establishing an accurate FE model capable of providing further insight into the shear behaviour of the B-SCs. Then, the FE model, verified by experimental results, was applied to analyse the effect of the concrete strength, and the thickness and tensile strength of the shear plate on the shear behaviour of the B-SCs. Finally, based on the results of push-out tests and FE analysis, calculation formulae for the ultimate shear resistance and slip modulus of the B-SCs were proposed.

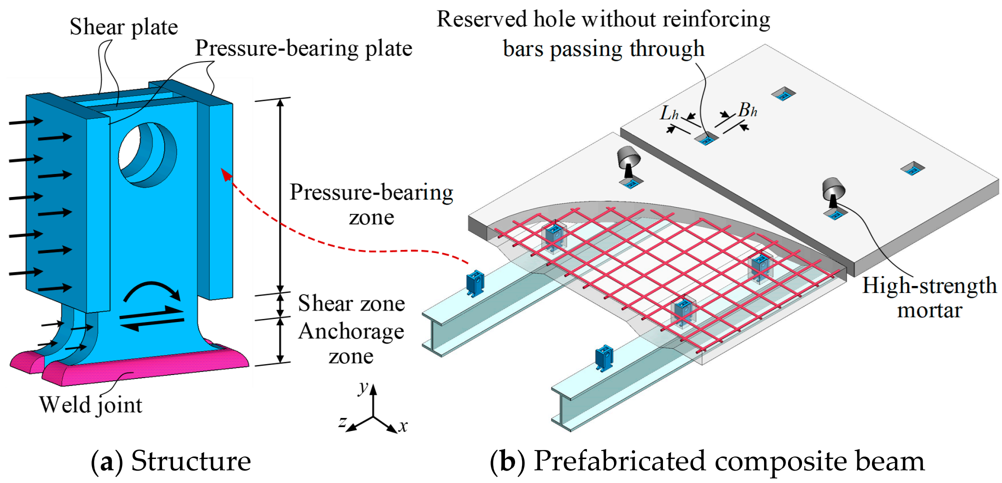

Figure 1. Bearing-shear connector (B-SC).

2. Summary of Push-Out Tests

Fifteen push-out specimen tests were performed by Zou [25] to study the effect of the geometry of B-SCs on their shear behaviour. Figures 2 and 3 show the test setup and geometric dimensions of the specimens manufactured in accordance with Eurocode 4 [31], respectively.

Each push-out specimen consisted of a 620 mm high H-steel beam (260 × 160 × 20 × 20 mm), two precast concrete slabs (500 mm × 300 mm × 650 mm), and two B-SCs. The pressuring-bearing plates and shear plates were made of Q345 and Q420, respectively [32]. Full penetration welding and fillet welding were used between the B-SCs and the steel beams, shear plates and pressure-bearing plates, respectively. The weld leg length of fillet welding was 16 mm. Figure 4 shows the structural details of the B-SCs.

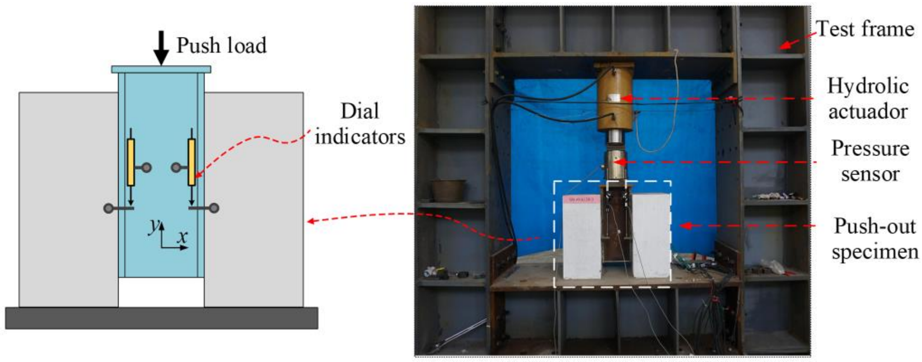

Figure 2. Test setup.

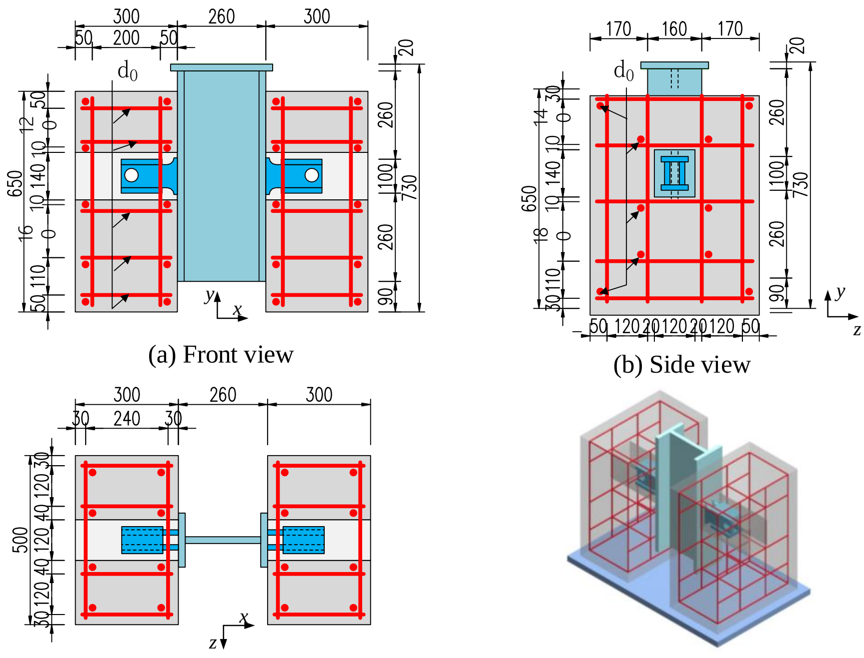

Figure 3. Geometry and dimensions of the specimens (mm).

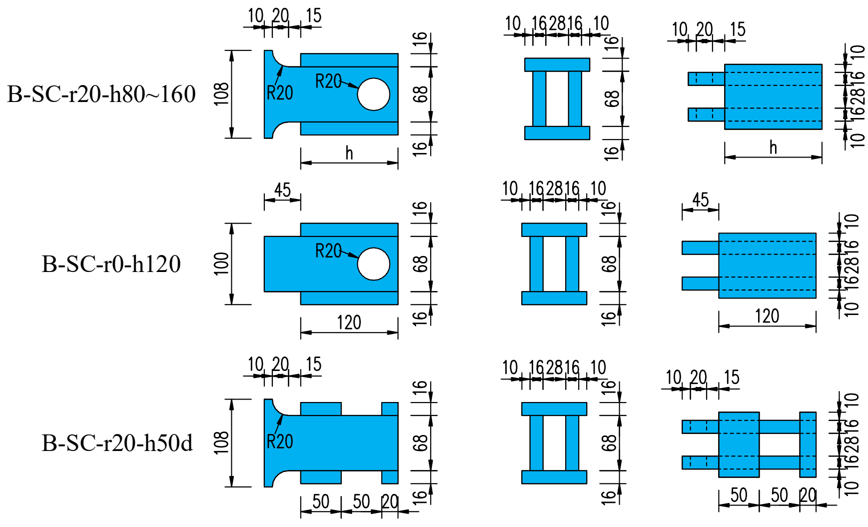

Figure 4. Details of the B-SCs (mm).

Each precast concrete slab had a reserved hole (120 × 140 mm) to accommodate the B-SCs and non-shrinkage high-strength mortar was cast into the reserved hole to achieve the composite action. Take the specimen B-SC-r20-h120 as an example; "r20" denotes the radius of the chamfer of the shear plate to 20; "h120" denotes the height of the pressure-bearing plate to 120.

3. Finite-Element Modelling

3.1. Geometry Model and Mesh

The general static-analysis method available in ABAQUS [33] was applied to model push-out tests [27–29]. A quarter FE model was developed for the biaxial symmetry of the specimens, as shown in Figure 5. The FE model considered the material and geometric nonlinearities. Taking the specimen B-SC-r20-h120 as an example, the complete process of FE modelling was introduced in detail.

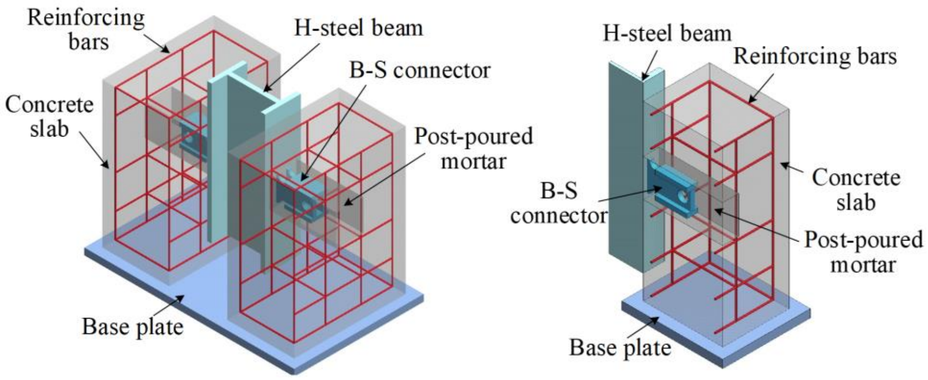

(**a**) Full FE model (**b**) Quater FE model

Figure 5. Geometry model of the push-out specimens.

As shown in Figure 6, three types of elements were applied for meshing. The B-SC, concrete slab, post-poured mortar, and steel beam were meshed with solid elements (C3D8R), which not only prevented shear-locking difficulties but also provided reasonable accuracy when compared with other element types [27–29]. The reinforcing bars were meshed using truss elements (T3D2) [27–29]. The rigid element (R3D4) was meshed the for base plate. The mesh size varied with the geometric size and importance of different parts. For example, the global and local seed sizes for the concrete slab and steel beam were 15 and 5 mm, respectively. To maintain the continuity of the element sizes and improve the convergence of the FE model, the mesh sizes of the B-SC and reinforcing bars were 5 and 15 mm, respectively.

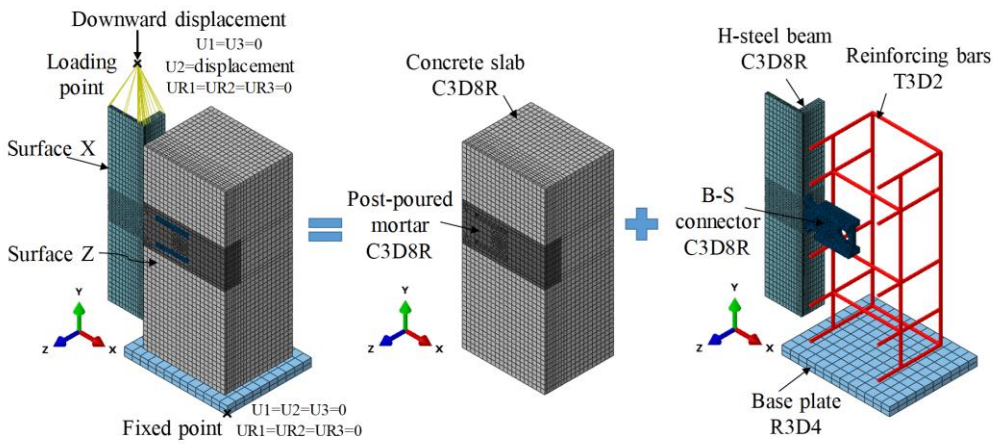

Figure 6. FE model and mesh.

3.2. Boundary Conditions and Loading Protocol

Symmetric boundary conditions were considered in the quarter FE model. As presented in Figure 6, all nodes on Surfaces X and Z were restrained from moving in the X and Z direction, respectively. The base plate was assumed fixed. A downward enforced displacement in the Y-direction was applied at the "Loading point".

3.3. Contact Modelling

In this study, two types of contact properties were employed for the interaction. First, contact interactions were used at the interface of the above-mentioned components, as shown in Figure 7. The normal "hard" contact and tangential "penalty" frictional formulation were considered for the first contact interaction. The friction coefficient between the steel beam and concrete slab was 0.6 [27,28], and that between the other components was 0.25 [28,29]. The reinforcing bars were "embedded" in their surrounding concrete.

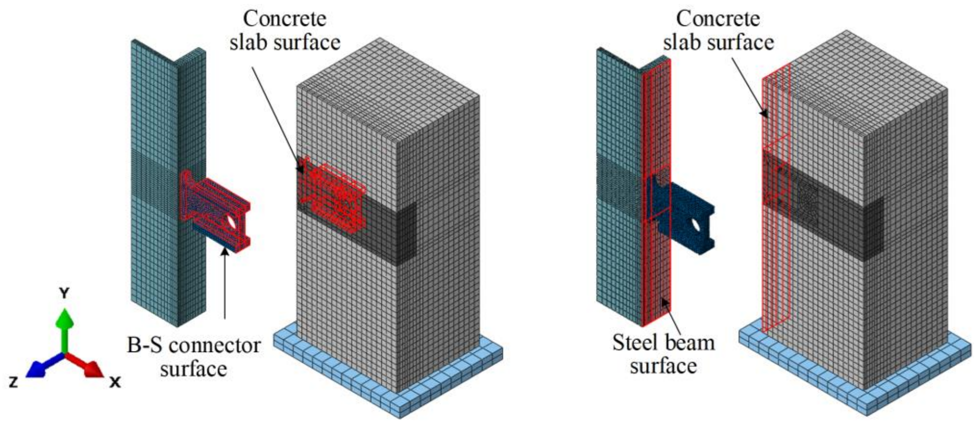

Figure 7. Contact modelling.

Second, the bonding force of the S-C interface significantly impacts the initial slip modulus of the connectors in push-out tests [27,34]. Therefore, the influence of the bonding force of the S-C interface on the shear performance of the B-SC should be considered. In addition to the first-contact property, surface-based cohesive behaviour was adopted to model the bonding force between the steel beam and concrete slab [34]. The bilinear traction–separation relationship was used to model the cohesive behaviour, as illustrated in Figure 8 [28,34,35]. The traction–separation model initially assumes a linear elastic behaviour, followed by the initiation and evolution of damage [35]. The uncoupled traction-separation type is given by Equation (1):

$$\boldsymbol{t} = \begin{Bmatrix} t_{\mathrm{n}} \\ t_{\mathrm{s}} \\ t_{\mathrm{t}} \end{Bmatrix} = \begin{bmatrix} K_{\mathrm{nn}} & 0 & 0 \\ 0 & K_{\mathrm{ss}} & 0 \\ 0 & 0 & K_{\mathrm{tt}} \end{bmatrix} \begin{Bmatrix} \delta_{\mathrm{n}} \\ \delta_{\mathrm{s}} \\ \delta_{\mathrm{t}} \end{Bmatrix} = \boldsymbol{K\delta} \quad (1)$$

According to the findings of a previous study [34], the parameters of cohesive behaviour were applied as follows: K_{nn} was considered as 0.05 E_{cm}, K_{ss}, and K_{tt} were considered as 0.05 G_{cm}, where E_{cm} and G_{cm} are the elastic and shear modulus of concrete, respectively. K_{nn}, K_{ss}, and K_{tt} are the elastic stiffness of the cohesive contact property [35]. The quadratic-stress criterion shown in Equation (2) was used as the damage-initiation criterion for cohesive behaviour. The parameters associated with the damage to cohesive behaviour were determined as follows: $t_{\mathrm{n}}^{0} = 0.05$, $t_{\mathrm{s}}^{0} = t_{\mathrm{t}}^{0} = 0.3$ [34,35] and $\delta_{\mathrm{n}}^{\mathrm{f}} = 0.8$ mm [34]; t_{n}, t_{s} and t_{t} are the tractions of the cohesive contact property [35].

$$\left(\frac{\langle t_{\mathrm{n}} \rangle}{t_{\mathrm{n}}^{0}}\right)^{2} + \left(\frac{\langle t_{\mathrm{s}} \rangle}{t_{\mathrm{s}}^{0}}\right)^{2} + \left(\frac{\langle t_{\mathrm{t}} \rangle}{t_{\mathrm{t}}^{0}}\right)^{2} = 1 \quad (2)$$

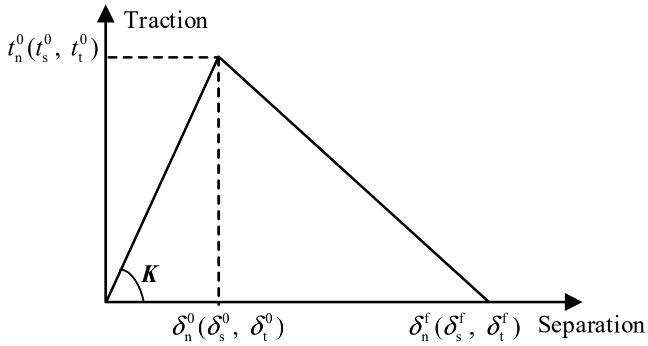

Figure 8. Typical traction and separation response.

3.4. Material Models

3.4.1. Concrete

"Concrete Damaged Plasticity" (CDP) was employed to model the uniaxial behaviour of concrete, as shown in Figure 9 [35]. The CDP assumes that the two primary failure modes of concrete are tensile cracking and compressive crushing, which are highly consistent with the failure modes of the concrete in these specimens.

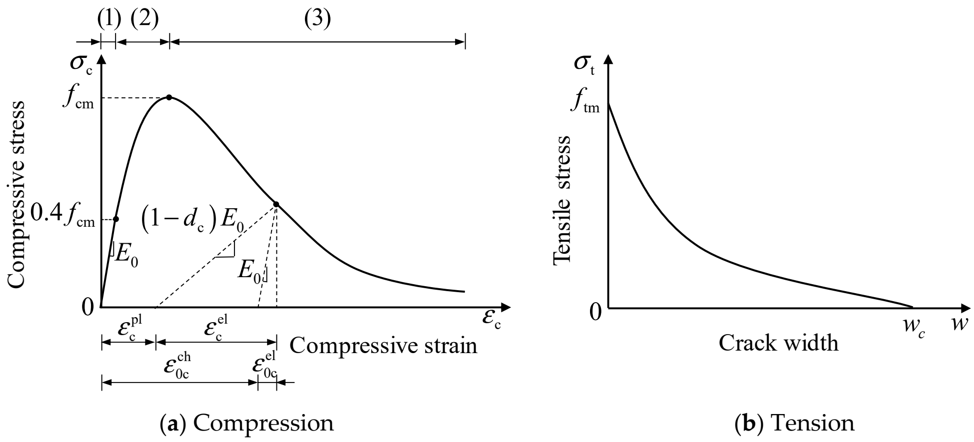

Figure 9. Concrete uniaxial behaviour.

Figure 9a,b present the uniaxial compression and tension behaviours of concrete, respectively. The stress–strain curve of the concrete under uniaxial compression is separated into three stages, as illustrated in Figure 9a. The first stage is linear ($0 \leq \sigma_c \leq 0.4f_{cm}$) [36].

$$\sigma_{c\ (1)} = E_{cm}\varepsilon_c \tag{3}$$

In Equation (3), σ_c and ε_c are the compressive stress and compressive strain of concrete, respectively; f_{cm} is the cylinder compressive strength of concrete. The cylinder compressive strength of concrete and non-shrinkage high-strength mortar were 44.5 MPa and 55.7 MPa, respectively. E_{cm} is the concrete elastic modulus, $E_{cm} = E_0\alpha_E(f_{cm}/10)^{1/3}$, $E_0 = 21.5$ GPa, and $\alpha_E = 1.0$. E_0 and α_E are the undamaged concrete elastic modulus and concrete aggregates factor, respectively. The second (ascending) stage is quadratic ($0.4f_{cm}<\sigma_c \leq f_{cm}$) [37].

$$\sigma_{c\ (2)} = -\left(\frac{k\eta - \eta^2}{1+(k-2)\eta}\right)f_{cm} \tag{4}$$

In Equation (4), $k = E_{cm}\varepsilon_{cm}/f_{cm}$. The peak strain ε_{cm} corresponding to the peak stress f_{cm} was equal to 0.025 [36]. $\eta(= \varepsilon_c/\varepsilon_{cm})$ is a coefficient. The third (descending) stage considers the dependency of the specimen geometry to ensure almost mesh-independent simulation results [37,38]:

$$\sigma_{c\ (3)} = \left(\frac{2 + \gamma_c f_{cm} \varepsilon_{cm}}{2 f_{cm}} - \gamma_c \varepsilon_c + \frac{\varepsilon_c^2 \gamma_c}{2 \varepsilon_{cm}} \right)^{-1} \tag{5}$$

$$\gamma_c = \frac{\pi^2 f_{cm} \varepsilon_{cm}}{2\left[\frac{G_{ch}}{l_{ck}} - 0.5 f_{cm}\left(\varepsilon_{cm}(1-b) + b\frac{f_{cm}}{E_0}\right)\right]^2} \tag{6}$$

In Equation (6), G_{ch} represents the crushing energy per unit area, $G_{ch} = (f_{cm}/f_{tm})^2 G_f$; f_{tm} is the tensile strength of concrete and is given in the literature [39,40]; G_f represents the fracture energy per unit area, $G_f = 0.073 f_{cm}^{0.18}$ (N/mm) [38]. l_{ck} is the characteristic element length, which depends on the type of element and mesh size. For three-dimensional solid elements, l_{ck} is the cube root of the element volume [37]. The value of b ($\varepsilon_c^{pl}/\varepsilon_c^{in}$) was 0.7, assuming that the majority of the inelastic compressive strain remained after unloading [37]. ε_c^{pl} and ε_c^{pl} are the compressive plastic strain and compressive inelastic strain of concrete, respectively.

The tensile behaviour of concrete exhibited two distinct stages. When the principal tensile stress of concrete did not exceed its peak tensile stress, no cracks in the concrete were assumed, and uncracked concrete kept elastic under tension. For cracked concrete, ABAQUS expresses the tensile-softening behaviour of concrete in three ways: stress–strain, tensile stress-crack width, and fracture energy [35]. A nonlinear tensile stress-crack width equation was applied to express the tensile brittle behaviour of concrete in this study [39–41].

$$\frac{\sigma_t}{f_{tm}} = \left[1 + \left(c_1 \frac{w}{w_c}\right)^3\right] \exp\left(-c_2 \frac{w}{w_c}\right) - \frac{w}{w_c}\left(1 + c_1^3\right) \exp(-c_2) \tag{7}$$

In Equation (7), c_1 = 3 and c_2 = 6.93 [37,38], where w_c is the cracking width corresponding to the zero tensile stress and $w_c = 5.14 G_f/f_{tm}$. The concrete-compression damage variable d_c and the tensile-damage variable d_t are used to express the deterioration of the concrete under compression and tension (Figure 10), respectively, and are given by Equations (8) and (9):

$$d_c = 1 - \frac{1}{2 + \alpha_c}\left[2(1 + \alpha_c) \exp\left(-b_c \varepsilon_c^{ch}\right) - \alpha_c \exp\left(-2 b_c \varepsilon_c^{ch}\right)\right] \tag{8}$$

$$d_t = 1 - \frac{1}{2 + \alpha_t}\left[2(1 + \alpha_t) \exp\left(-b_t \varepsilon_t^{ck}\right) - \alpha_t \exp\left(-2 b_t \varepsilon_t^{ck}\right)\right] \tag{9}$$

$$b_c = \frac{1.97 f_{cm}}{G_{ch}} l_{ck} \tag{10}$$

$$b_t = \frac{0.453 (f_{cm} - 8)^{2/3}}{G_f} l_{ck} \tag{11}$$

In Equations (8) and (9), $\alpha_c = 7.873$, $\alpha_t = 1$ $\varepsilon_c^{ch} = \varepsilon_c - \sigma_c/E_0$, $\varepsilon_t^{ck} = \varepsilon_t - \sigma_t/E_0$, $\varepsilon_t = \varepsilon_{tm} - w/l_{ck}$, where α_c, α_t, b_c, and b_t are the dimensionless coefficients, ε_{tm} is the tensile peak strain of concrete. ε_c^{ch} and ε_t^{ck} are the compressive crushing strain and tensile cracking strain of concrete, respectively.

To accurately define the plastic-damage model of concrete, the following five additional parameters are required: dilation angle ψ = 37° [13]; flow potential eccentricity ε = 1; raio of biaxial to uniaxial compressive strength σ_{bo}/σ_{co} = 1.16; ratio of K = 2/3, and viscosity parameter μ = 0.005 [34]. The application of the CDP yields an unsymmetric material-stiffness matrix. Thus, an unsymmetric matrix storage and solution scheme should be adopted in the step module to achieve an appropriate convergence rate in ABAQUS [35].

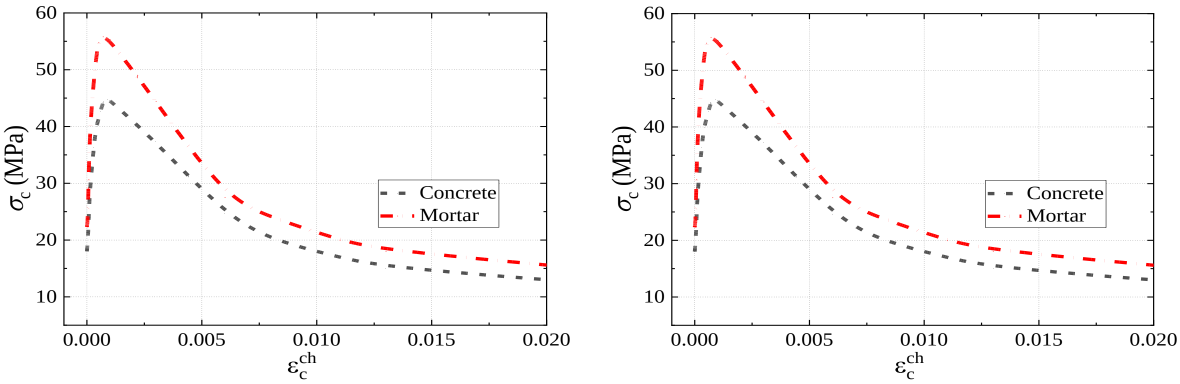

(**a**) Compressive stress vs. crushing strain (**b**) Tensile stress VS crack width

Figure 10. Material constitution of concrete.

3.4.2. Steel Materials

The yield strength, ultimate tensile strength, and elastic modulus of Q345 were 361.3 MPa, 479.6 MPa, and 200.3 GPa, respectively. The yield strength, ultimate tensile strength, and elastic modulus of Q420 were 449.6 MPa, 600.2 MPa, and 201.5 GPa, respectively. HRB400 was used for the reinforcing bars, and the yield strength, ultimate tensile strength, and elastic modulus of HRB400 were 439.3 MPa, 577.1 MPa, and 203.7 GPa, respectively.

Figure 11 presents the stress–strain relationship for steel. As shown in Figure 11a, the descending branch of the stress–strain curve of the shear plate was used to simulate shear-plate failure [27,30]. The ultimate strain ε_u and fracture strain ε_f of the shear plate used in the FE model were 0.13 and 0.135, respectively. As shown in Figure 11b, the ideal elastoplastic bilinear model was adopted to model other steel components except the shear plate [30,31].

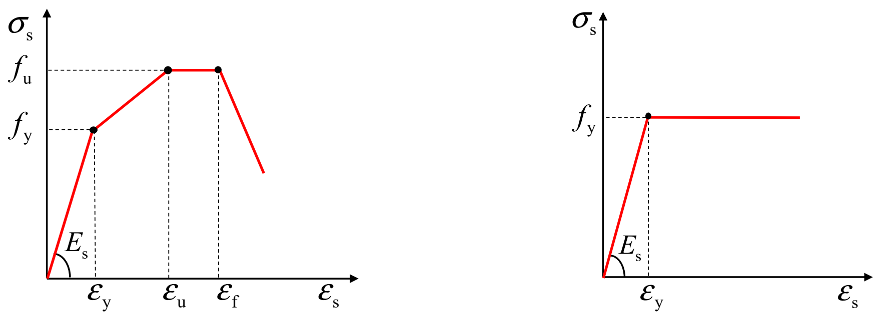

(**a**) Shear plate (**b**) Steel beam, pressure-bearing plate, and reinforcing bars

Figure 11. Stress–strain relationship of steel.

4. Verification of the Numerical Model

4.1. Comparison of Shear Resistance and Slip Modulus

The results of push-out tests were used to validate the effectiveness of the numerical model. A comparison between the ultimate shear resistance and slip modulus of the B-SCs in tests and numerical analysis, listed in Table 1, shows a high agreement for all push-out specimens, with a maximum deviation of 6% found for B-SC-r20-h160-3. The mean value of $P_{u,\ test}/P_{u,\ FE}$ was 0.99 with a standard deviation of 0.03 and the mean value $K_{0.2,\ test}/K_{0.2,\ FE}$ was 1.00 with a standard deviation of 0.03. This demonstrates that the established numerical model can effectively perform a parametric study on the shear resistance and slip modulus of the B-SCs.

Table 1. Comparison between experimental results and FE results.

Specimens	$P_{u,test}$ (kN)	$P_{u,FE}$ (kN)	$K_{0.2,test}$ (kN/mm)	$K_{0.2,FE}$ (kN/mm)	$\frac{P_{u,\,test}}{P_{u,\,FE}}$	$\frac{K_{0.2,\,test}}{K_{0.2,\,FE}}$
B-SC-r20-h120-1	1230.0	1217.4	2076.2	2073.7	1.01	1.00
B-SC-r20-h120-2	1210.5		2013.7		0.99	0.97
B-SC-r20-h120-3	1162.2		1997.6		0.95	0.96
B-SC-r20-h80-1	1180.9	1135.8	1987.3	2008.2	1.04	0.99
B-SC-r20-h80-2	1146.2		2056.6		1.01	1.02
B-SC-r20-h80-3	1089.6		2051		0.96	1.02
B-SC-r20-h160-1	1231.5	1219.0	2051.2	2060.7	1.01	1.00
B-SC-r20-h160-2	1180.1		1984.7		0.97	0.96
B-SC-r20-h160-3	1140.9		1927.9		0.94	0.94
B-SC-r20-h50d-1	1228.1	1216.7	2142.3	2075.7	1.02	1.03
B-SC-r20-h50d-2	1198		2165.0		0.94	1.04
B-SC-r20-h50d-3	1197.6		2125.1		0.97	1.02
B-SC-r0-h120-1	1168.8	1149.2	1975.4	1940.0	1.01	1.02
B-SC-r0-h120-2	1079.2		1928.7		0.98	0.99
B-SC-r0-h120-3	1116.1		1951.6		0.98	1.01
Mean					0.99	1.00
Standard deviation					0.03	0.03

where P_u is the ultimate shear resistance and $K_{0.2}$ is the secant slope of the load-slip curves at a slip of 0.2 mm.

4.2. Comparison of Load-Slip Curves

As shown in Figure 12, the load-slip curves derived from the FE model were observed to be in close agreement with the push-out tests. Figure 12 also reveals that the load-slip curves of all push-out specimens followed a similar trend, and they can be divided into three distinct stages. At the initial elastic stage, the shear load increased rapidly with little slip, indicating that the B-SCs had a high slip modulus at the initial stage. Subsequently, the slip increased rapidly, while the shear load slowly increased to the peak load. Finally, the load gradually decreased as the slip continued to increase. Therefore, the FE model can effectively evaluate the overall trend of the load-slip curves of the B-SCs.

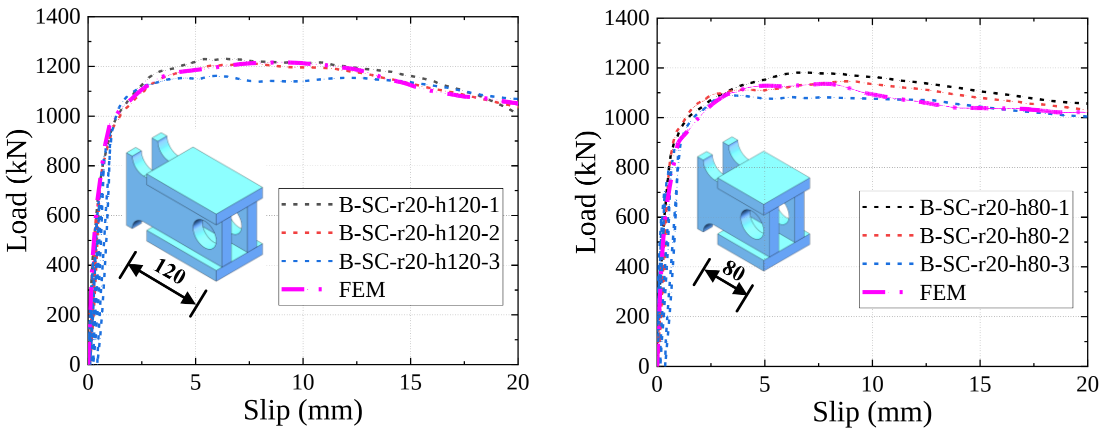

(**a**) B-SC-r20-h120 (**b**) B-SC-r20-h80

Figure 12. *Cont.*

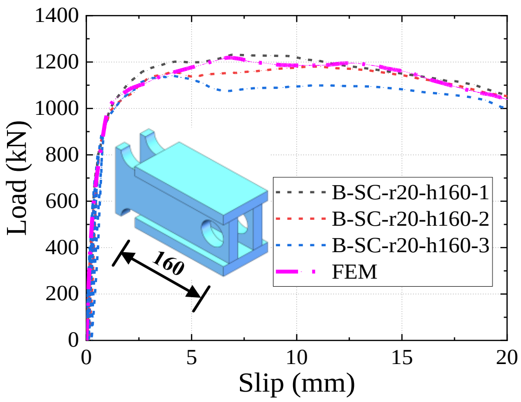

(**c**) B-SC-r20-h160

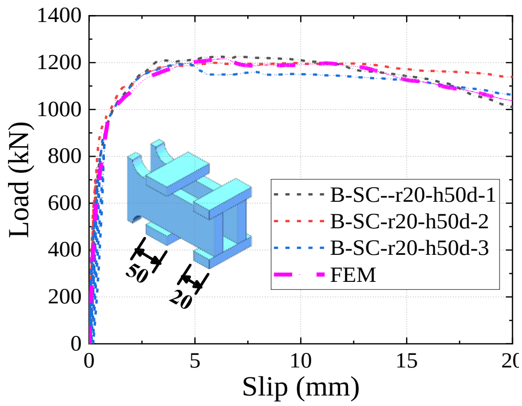

(**d**) B-SC-r20-h50d

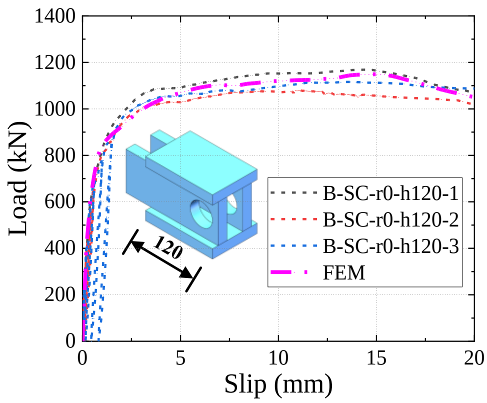

(**e**) B-SC-r0-h120

Figure 12. Comparison of load-slip curves.

4.3. Comparison of Failure Modes

As shown in Figure 13, the failure modes derived from the FE model closely matched those observed in push-out tests. The distribution and development law of the concrete-slab cracks in the FE model matched well with the experimental response. As illustrated in Figure 13b, the shear plate exhibited significant shear deformation along the loading direction in both the experiments and FE modelling, whereas the pressure-bearing plate exhibited no evident deformation. According to the studies reported above, the FE model can accurately predict the shear behaviour of the B-SCs.

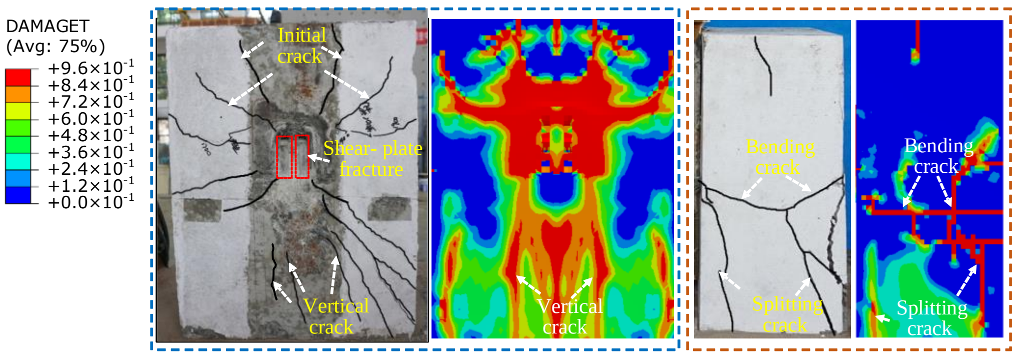

(**a**) Crack distribution of the concrete slab

Figure 13. *Cont.*

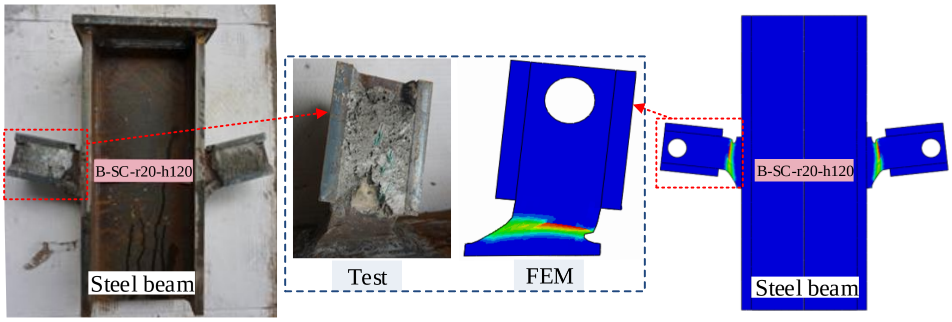

(**b**) Deformation of the B-SC

Figure 13. Failure modes of the specimen B-SC-r20-h120.

4.4. Failure Process of B-SCs

In Section 4.3, the failure modes of the push-out specimens were primarily proved as splitting and shear failures of the concrete slab and shear plate, respectively. In addition, push-out tests have demonstrated that shear deformation of the shear plate provides the majority of the shear resistance of the B-SCs [25]. Therefore, an analysis of the failure mechanisms of concrete slabs and shear plates is necessary.

According to the B-SC-r20-h120 FE model, the complete failure process of the B-SCs was analysed as follows. The load-slip curve for specimen B-SC-r20-h120 is shown in Figure 14, on which five typical points are marked, with points I and II representing the elastic stage and points III and IV representing the elastic–plastic stage, and point V representing the ultimate state [42]. Figure 15 presents the deformation of the concrete slab and the stress of the shear plate at these five key points, which illustrates the complete failure process of the push-out specimens in detail.

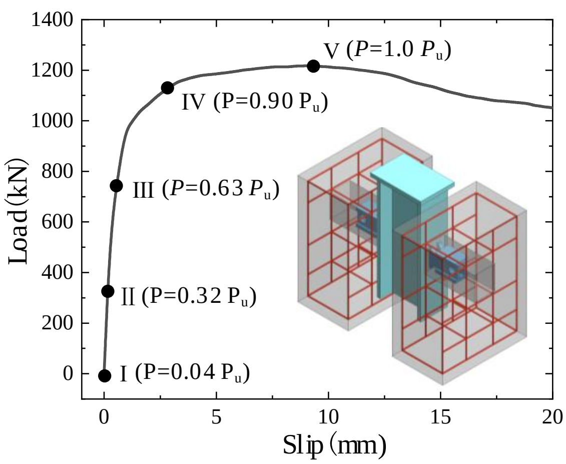

Figure 14. Load-slip curve of the specimen B-SC-r20-h120 (FE model).

When P = 0.04 P_u and slip = 0.02 mm, the specimen exhibited the elastic stage. As shown in Figure 15a, the shear-plate stress did not exceed 20 MPa, and no cracks appeared in the concrete slab.

When P = 0.32 P_u and slip = 0.18 mm, the specimen still exhibited an elastic response. The stress in the anchorage and shear zones of the B-SC was significantly greater than that in other areas, as illustrated in Figure 15b. In addition, the concrete slab at the root of the B-SC exhibited small cracks owing to the extrusion of the shear plate, which is consistent with the phenomenon of splitting cracks in the concrete slab owing to the extrusion of the stud connector [11].

When P = 0.63 P_u and slip = 0.58 mm, plastic deformation occurred locally in the push-out specimen. As shown in Figure 15c, the local stress in the anchorage and shear zones of the B-SC was larger than the yield strength owing to the combined action of bending and shear. The existing cracks in the concrete slab near the B-SC continued to extend under the action of the load and the cracked area extended from the post-poured high-strength mortar to the precast concrete slab.

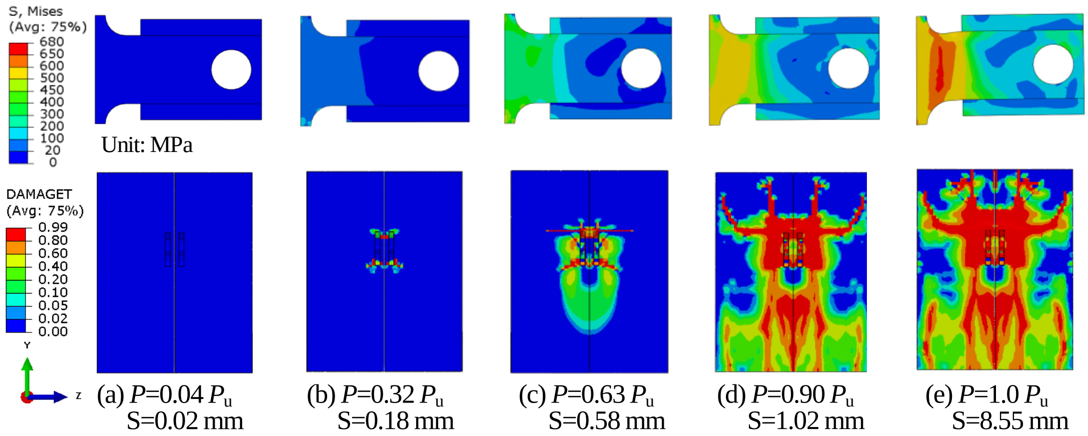

Figure 15. Deformation and stress distribution of concrete slab and shear plate.

When P = 0.90 P_u and slip = 2.27 mm, as shown in Figure 15d, the stress in the shear-plate zone was greater than the yield strength. Cracks in the concrete slab developed significantly and cracks near the B-SC extended to the bottom and top of the concrete slab.

When P = 1.0 and slip = 8.55 mm, the specimen reached its ultimate state. The local stress in the shear zone of the B-SC reached the ultimate tensile strength of steel, as shown in Figure 15e. The stress in the anchorage zone was less than that in the shear zone, which ensured that the failure of the shear zone of the B-SC preceded that of the anchorage zone. At this time, the cracks spread throughout the precast concrete slab, indicating that the B-SC reached the ultimate state, mainly because the cracked concrete slab was insufficient to support the increase in load.

5. Parametric Study

The effect of the following factors on the shear behaviour of the B-SCs were investigated in the parametric study: concrete strength, the thickness and the tensile strength of the shear plate, and stirrup diameter, as shown in Figure 16.

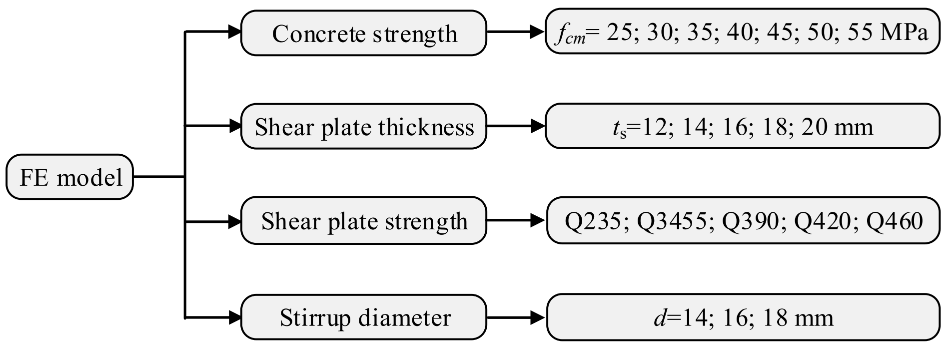

Figure 16. FE models evaluated in parametric study.

5.1. Effect of Concrete Strength

As shown in Figure 17a, when the numerical model included and excluded the postpoured high-strength mortar, the two load-slip curves almost coincided, which was consistent with Yu's conclusion [43]. For conservatism and simplicity, high-strength mortar was not included in the subsequent parametric analysis. A comparison of the load-slip curves for different concrete strengths (25 MPa–55 MPa) [36] is illustrated in Figure 17b.

As shown in Figure 17b,c, the ultimate shear resistance and slip modulus of the B-SCs increased as the concrete strength increased. According to Figure 17b, the ductility of the B-SCs also increased as the concrete strength increased, which confirmed the conclusion of Oehlers [44].

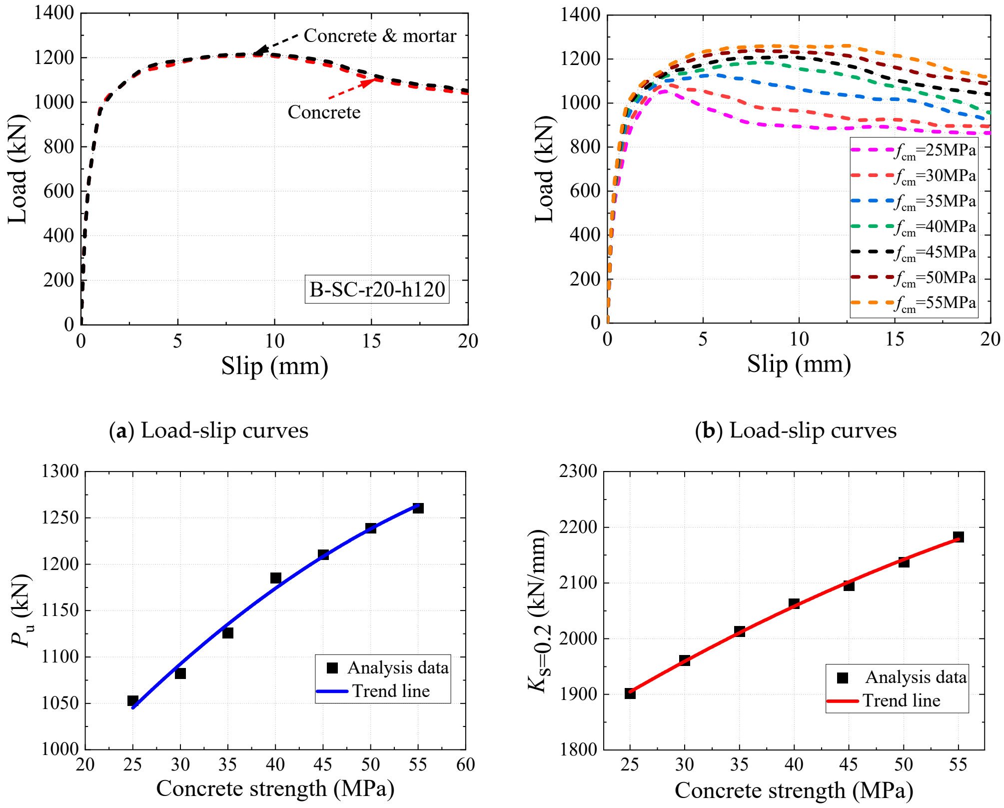

(**a**) Load-slip curves (**b**) Load-slip curves

(**c**) Impact analysis of shear resistance (**d**) Impact analyses of slip modulus

Figure 17. Effect of concrete strength.

Figure 18 presents the stress distribution of the B-SCs for different concrete strengths in the ultimate state. When the concrete strength increased, the shear deformation and high-stress area of the shear plate in the ultimate state also increased. This can be attributed to the increase in the cracking resistance of a precast concrete slab with the increase in concrete strength. Higher-strength concrete enables concrete to support greater shear deformation of the shear plate, which increases the contribution of the shear plate to the shear resistance of B-SCs, thereby improving the ultimate shear resistance of B-SCs.

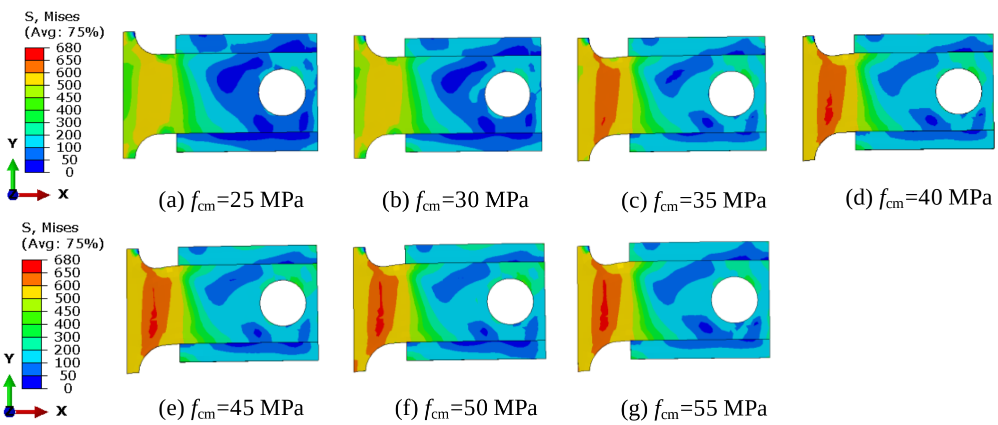

Figure 18. Stress-cloud diagram of B-SCs on the ultimate state (MPa).

5.2. Effect of Shear-Plate Thickness

Previous experimental studies have demonstrated a significant impact of the diameter of studs and bolts on their ultimate shear resistance [45,46]. Similarly, Table 2 demonstrates the significant impact of shear-plate thickness on the ultimate shear resistance and but a negligible impact on the slip modulus of the B-SCs. As summarized in Table 2, the ultimate shear resistance and slip modulus increased by 42.5% and 2.2%, respectively, when the shear-plate thickness increased from 12 to 20 mm. As illustrated in Figure 19b, the ultimate shear resistance increased approximately linearly with the shear plate thickness. Figure 19c presents the stress-cloud diagram of the shear plates for different thicknesses in the ultimate state. The shear deformation and high-stress area of the shear plate can be observed to have decreased as the shear-plate thickness increased. This may be attributable to the fact that increasing the shear-plate thickness can increase the effective shear-cross area of the shear plate, thereby lowering its shear deformation, increasing the bearing area of concrete, and improving the ultimate shear resistance of B-SCs.

Table 2. Results of FE parametric study.

Specimens	E_s (GPa)	f_y (MPa)	f_u (MPa)	Shear-Plate Thickness (mm)	$P_{u,FEM}$ (kN)	$K_{0.2,FEM}$ (kN/mm)
B-SC-shear-12				12	969.9	2041.2
B-SC-shear-14				14	1099.5	2058.6
B-SC-shear-16	201.5	449.6	600.2	16	1217.4	2073.4
B-SC-shear-18				18	1271.7	2077.6
B-SC-shear-20				20	1381.9	2086.7
B-SC-Q235	210	235	370		822.9	2073.4
B-SC-Q345	210	345	470		993.5	2073.4
B-SC-Q390	210	390	490	16	1030.6	2073.4
B-SC-Q420	210	420	520		1081.8	2073.4
B-SC-Q460	210	460	550		1142.2	2073.4

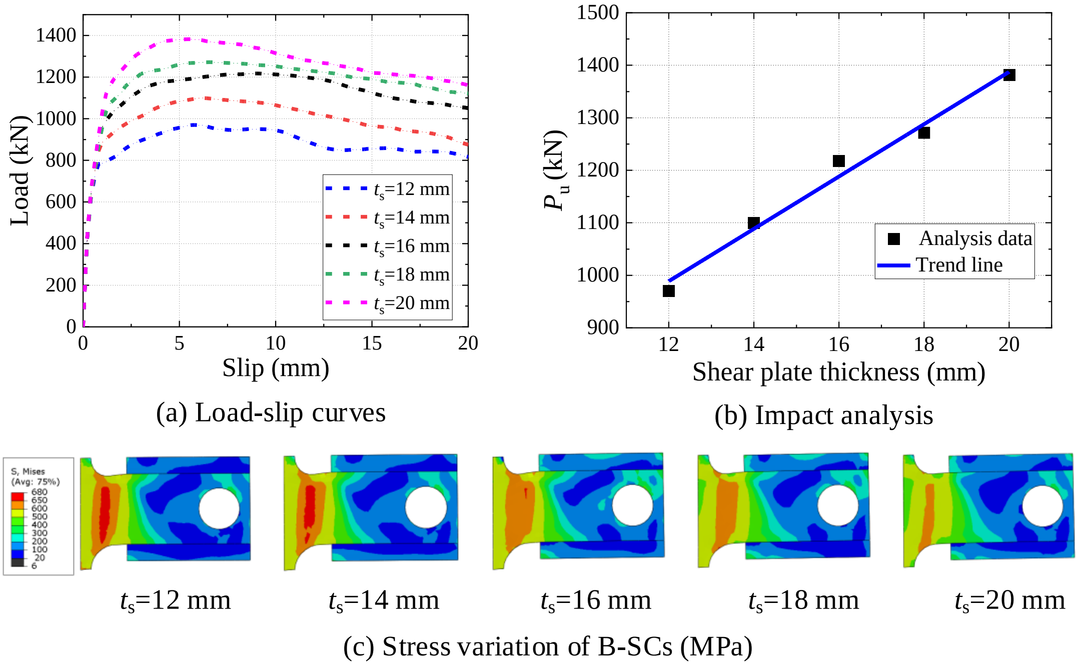

Figure 19. Effect of shear-plate thickness.

5.3. Effect of Shear-Plate Tensile Strength

According to GB 50017-2017 [32], five types of structural steel were selected for the parametric analysis, as listed in Table 2.

Figure 20 presents the effect of the shear-plate tensile strength on the shear behaviour of the B-SCs, and a comparison between the ultimate shear resistance and slip modulus of the specimens is summarised in Table 2. As depicted in Figure 20b, the ultimate shear resistance increased approximately linearly with the shear-plate tensile strength, whereas the slip modulus remained constant because the elastic modulus of steels with varying tensile strengths were nearly identical. The ultimate shear resistance increased by 38.8% when the steel type of the shear plate was changed from Q235 to Q460, indicating the significant impact of the shear-plate tensile strength on the ultimate shear resistance of the B-SCs.

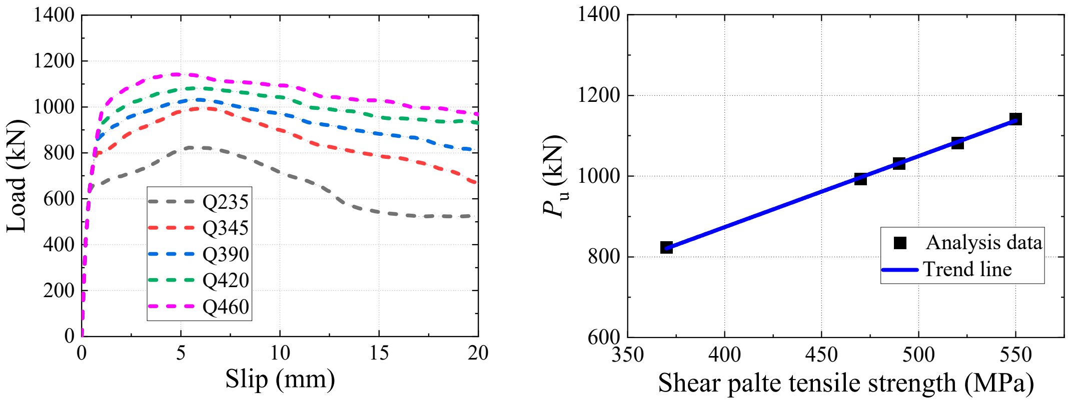

(**a**) Load-slip curves (**b**) Impact analysis

Figure 20. Effect of shear-plate tensile strength.

5.4. Effect of Stirrup Diameter

The confinement of stirrup to concrete slabs has been demonstrated to significantly affect the behaviour of shear connectors [42,47]. Figure 21 presents the effect of the stirrup diameter on the shear behaviour of the B-SCs and a comparison between the ultimate shear resistance and slip modulus is summarised in Table 3. The ultimate shear resistance improved by 1.7% when the stirrup diameter d increased from 14 to 18 mm, but the slip modulus remained constant because the stirrup had not imposed its confinement action on concrete when the relative slip was 0.2 mm.

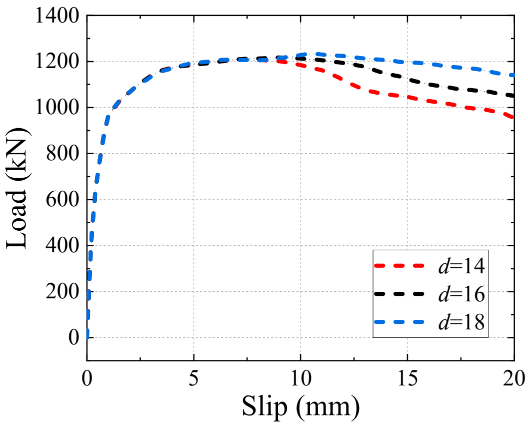

Figure 21. Effect of stirrup diameter.

Table 3. Results of FE parametric analysis.

Specimen	*d* mm	P_u (kN)	$K_{0.2}$ (kN/mm)
B-SC-stirrup-14	14	1212.3	2070.3
B-SC-stirrup-16	16	1217.4	2070.3
B-SC-stirrup-18	18	1232.9	2070.3

6. Proposed Shear-Calculation Formulae and Validation

6.1. Proposed Formula for Predicating Ultimate Shear Resistance

According to Sections 4.3 and 4.4, the failure modes of the push-out specimens with B-SCs were primarily the splitting and shear failures of the concrete slab and shear plate, respectively, indicating the primarily affected shear resistance of the B-SCs by the properties of the concrete slab and shear plate. Figure 22 presents the shear mechanism of the B-SCs. A parametric study showed that the concrete strength (f_{cm}), the thickness (t_s), and the tensile strength (f_u) of the shear plate had a significant impact on the ultimate shear resistance. Especially, the concrete strength directly affects the shear deformation of the shear plate. Therefore, introducing a coefficient $\lambda_s \left(= \alpha \frac{E_{cm}}{f_{cm}} + \beta\right)$ was reasonable, which is related to the concrete-strength grade, to quantify the contribution of the shear plate to the ultimate shear resistance; α and β are the coefficients. Therefore, the new design formula for the ultimate shear resistance of B-SCs was suggested as follows [25]:

$$P_u = V_{s,s} + P_{b,a} \tag{12}$$

$$V_{s,s} = \lambda_s A_{s,s} f_u \tag{13}$$

$$P_{b,a} = \lambda_b A_{b,a} \sqrt{E_{cm} f_{cm}} \tag{14}$$

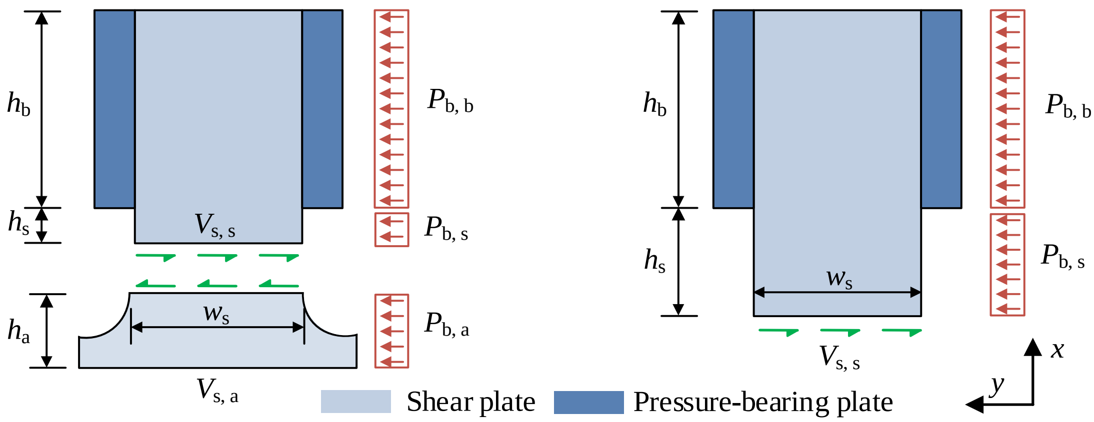

(**a**) Widening shear plate (**b**) Rectangular shear plate

Figure 22. Shear mechanism of B-SCs.

Based on the results of tests and FE parametric study, the values of α and β are 0.0003 and 0.82, respectively, when the least-squares method is used. In Equation (12), $V_{s,s}$ is the shear capacity of the shear zone and $P_{b,a}$ is the compressive capacity of concrete in the anchorage zone. In Equation (13), $A_{s,s}$ ($t_s w_s$) is the cross-sectional area of the shear zone, and t_s, w_s, and f_u are the thickness, width, and tensile strength of the shear plate, respectively. λ_b (=0.052) is a constant coefficient [25], and $A_{b,a}$ is the local bearing area of the anchoring zone. f_{cm} and E_{cm} are the compressive cylinder strength and elastic modulus of concrete, respectively.

The proposed ultimate shear-resistance formula for B-SCs was validated by comparing it with the results of experiments and FE parametric analysis in Tables 4 and 5, and Figure 23a. The mean value of $P_{\mathrm{u,\,pre}}/P_{\mathrm{u,\,test}}$ was 0.99 with a standard deviation of 0.037; the mean value of $P_{\mathrm{u,\,pre}}/P_{\mathrm{u,\,FEM}}$ was 0.98 with a standard deviation of 0.048, indicating that the proposed design formula can accurately predict the ultimate shear resistance of B-SCs.

Table 4. Comparison between predicted values and tests.

Tests Specimens	$P_{\mathrm{u,test}}$ **(kN)**	$P_{\mathrm{u,pre}}$ **(kN)**	$K_{0.2,\mathrm{test}}$ **(kN/mm)**	$K_{0.2,\mathrm{pre}}$ **(kN/mm)**	$\frac{P_{\mathrm{u,\,pre}}}{P_{\mathrm{u,\,test}}}$	$\frac{K_{0.2,\,\mathrm{pre}}}{K_{0.2,\,\mathrm{test}}}$
B-SC-r20-h120-1	1230.0	1182.0	2076.2	2059.2	0.96	1.01
B-SC-r20-h120-2	1210.5	1182.0	2013.7	2059.2	0.98	0.98
B-SC-r20-h120-3	1162.2	1182.0	1997.6	2059.2	1.02	0.97
B-SC-r20-h80-1	1180.9	1182.0	1987.3	2059.2	1.00	0.97
B-SC-r20-h80-2	1146.2	1182.0	2056.6	2059.2	1.03	1.00
B-SC-r20-h80-3	1089.6	1182.0	2051	2059.2	1.08	1.00
B-SC-r20-h160-1	1231.5	1182.0	2051.2	2059.2	0.96	1.00
B-SC-r20-h160-2	1180.1	1182.0	1984.7	2059.2	1.00	0.96
B-SC-r20-h160-3	1140.9	1182.0	1927.9	2059.2	1.04	0.94
B-SC-r20-h50d-1	1228.1	1182.0	2142.3	2059.2	0.96	1.04
B-SC-r20-h50d-2	1198	1182.0	2165.0	2059.2	0.99	1.05
B-SC-r20-h50d-3	1197.6	1182.0	2125.1	2059.2	0.99	1.03
B-SC-r0-h120-1	1168.8	1088.0	1975.4	2059.2	0.93	0.96
B-SC-r0-h120-2	1079.2	1088.0	1928.7	2059.2	1.01	0.94
B-SC-r0-h120-3	1116.1	1088.0	1951.6	2059.2	0.97	0.95
Mean					0.99	0.99
Standard deviation					0.037	0.035

Table 5. Comparison between predicted values and FE analysis.

Parametric Study	**Specimens**	$P_{\mathrm{u,FE}}$ **(kN)**	$P_{\mathrm{u,pre}}$ **(kN)**	$K_{0.2,\mathrm{test}}$ **(kN/mm)**	$K_{0.2,\mathrm{pre}}$ **(kN/mm)**	$\frac{P_{\mathrm{u,\,pre}}}{P_{\mathrm{u,\,FE}}}$	$\frac{K_{0.2,\,\mathrm{pre}}}{K_{0.2,\,\mathrm{FE}}}$
Concrete strength	B-SC-f_{cm}-25	1053.0	1144.3	1901.7	1911.1	1.09	1.00
	B-SC-f_{cm}-30	1082.2	1154.6	1961.2	1951.9	1.07	1.00
	B-SC-f_{cm}-35	1126.3	1164.3	2013.4	1990.5	1.03	1.01
	B-SC-f_{cm}-40	1185.3	1173.7	2062.8	2027.4	0.99	1.02
	B-SC-f_{cm}-45	1210.6	1182.9	2095.3	2062.7	0.98	1.02
	B-SC-f_{cm}-50	1238.8	1191.7	2137.9	2096.7	0.96	1.02
	B-SC-f_{cm}-55	1260.7	1200.3	2183.0	2129.6	0.95	1.03
Shear-plate thickness	B-SC-shear-12	969.9	886.5	2041.2	2059.2	0.91	0.99
	B-SC-shear-14	1099.5	1034.2	2058.6	2059.2	0.94	1.00
	B-SC-shear-16	1217.4	1182.0	2073.4	2059.2	0.97	1.01
	B-SC-shear-18	1271.8	1329.7	2077.6	2059.2	1.05	1.01
	B-SC-shear-20	1382.0	1477.4	2086.7	2059.2	1.07	1.01
Shear-plate tensile strength	B-SC-Q235	823.0	764.9	2070.3	2059.2	0.93	1.01
	B-SC-Q345	993.5	946.2	2070.3	2059.2	0.95	1.01
	B-SC-Q390	1031.6	982.5	2070.3	2059.2	0.95	1.01
	B-SC-Q420	1081.8	1036.9	2070.3	2059.2	0.96	1.01
	B-SC-Q460	1142.2	1091.3	2070.3	2059.2	0.96	1.01
Stirrup diameter	B-SC-stirrup-14	1212.3	1182.0	2070.3	2059.2	0.97	1.01
	B-SC-stirrup-16	1217.4	1182.0	2070.3	2059.2	0.97	1.01
	B-SC-stirrup-18	1232.9	1182.0	2070.3	2059.2	0.96	1.01
Mean						0.98	1.01
Standard deviation						0.048	0.008

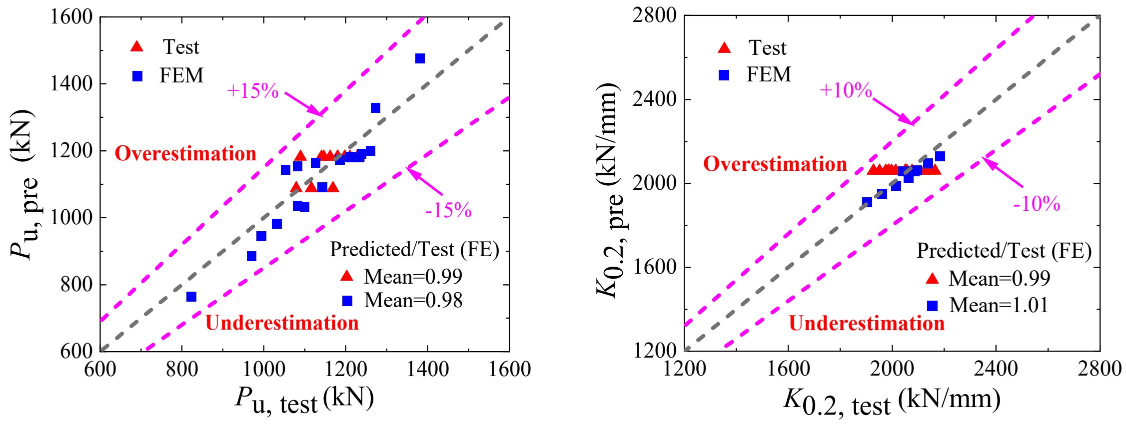

(**a**) Evaluation of shear resistance (**b**) Evaluation of slip modulus

Figure 23. Validation of the proposed design formulae.

6.2. Proposed Formula for Predicating Slip Modulus

The slip modulus of B-SCs is determined by the secant slope of the load-slip curves at a slip of 0.2 mm [48–50]. The advantage of this method is the fixed-slip value, and the calculation error caused by the relative dispersion of the test values of the ultimate shear resistance can be avoided. Shim [9] proposed a Formula (15) to predict the slip modulus of large-diameter studs. The formula considers the effect of concrete strength on slip modulus.

$$k_s = \frac{P_{max}}{d(0.16 - 0.0017 f_c)} \tag{15}$$

In JTG/T D64-01-2015 [51], the slip modulus of studs was expressed as Equation (16), which accounts for the contributions of the concrete elastic modulus, concrete strength, and stud diameter to the slip modulus. Hu [50] proposed a slip modulus design formula for large-diameter stud connectors, as expressed by Equation (17).

$$k_s = 13.0d\sqrt{E_c f_c} \tag{16}$$

$$k_s = 0.62d^2\sqrt{E_c f_c} \tag{17}$$

According to the parametric analysis, concrete strength directly affected the failure modes of the push-out specimens. Figure 17d shows a significant effect of concrete strength on slip modulus, while the shear-plate thickness had a minor effect on slip modulus. Therefore, the influence of the concrete strength on the slip modulus was quantified by introducing a parameter λ_k related to the concrete strength. A new formula for the slip modulus of B-SCs was proposed by regression analysis as follows:

$$K_{0.2} = (0.0016\frac{E_{cm}}{f_{cm}} + 0.37)\sqrt{E_{cm} f_{cm}} \tag{18}$$

In Equation (18), $\lambda_k = 0.0016E_{cm}/f_{cm}$. The proposed slip-modulus formula was validated by comparing the tests and FE analysis results in Tables 4 and 5, and Figure 23b. The mean value of $K_{0.2,\,pre}/P_{0.2,\,test}$ was 0.99 with a standard deviation of 0.035, and the mean value of $K_{0.2,\,pre}/P_{0.2,\,FE}$ was 1.01 with a standard deviation of 0.008, indicating that the proposed design formula can accurately evaluate the slip modulus of B-SCs.

7. Conclusions

In this study, a three-dimensional refined nonlinear numerical model was established to investigate the shear behaviour of B-SCs. Then, using the verified numerical model, the effects of the concrete strength and the thickness and the tensile strength of the shear plate on the shear behaviour of B-SCs were investigated. The following conclusions can be drawn:

1. The numerical model matched well with the push-out tests in terms of the ultimate shear resistance, slip modulus, load-slip curves, and failure modes, indicating the accurate evaluation of the shear behaviour of B-SCs in prefabricated composite structures using the numerical model;
2. All push-out specimens with B-SCs exhibited mixed failure modes composed of splitting and shear failures of the concrete slab and shear plate, respectively. The higher strength concrete enables concrete to support greater shear deformation of the shear plate, which increases the contribution of the shear plate to the shear resistance of B-SCs, thus improving the ultimate shear resistance of B-SCs;
3. The ultimate shear resistance of B-SCs increased approximately linearly with the increase in the thickness and the tensile strength of the shear plate because the shear resistance of B-SCs was mainly determined by the shear resistance of the shear plate. However, these two parameters had a minor influence on the slip modulus of B-SCs;
4. New calculation formulae for the ultimate shear resistance and slip modulus of the B-SCs were proposed. Both formulae, which accounted for the effect of concrete strength on the shear deformation of the shear plate, agreed well with the results of the push-out tests and numerical analysis.

Author Contributions: Z.Z. (Zhichao Zheng): Software, Validation, Writing. Y.Z.: Investigation. Y.C.: Supervision, Review. F.Q.: Writing, Funding acquisition. F.C.: Investigation. J.D.: Supervision, Review. Z.Z. (Zhigang Zhang): Investigation. All authors have read and agreed to the published version of the manuscript.

Funding: This work was supported by the National Natural Science Foundation of China (No. 52078081), Chongqing Technology Innovation and Application Development Project (No. CSTB2022TIAD-KPX0103, cstc2020jscx-msxmX0079).

Institutional Review Board Statement: Not applicable.

Informed Consent Statement: Not applicable.

Data Availability Statement: The data presented in this study are available on request from the corresponding author.

Conflicts of Interest: The authors declare that they have no known competing financial interests or personal relationships that could have appeared to influence the work reported in this paper.

Abbreviations

δ_n^f	Maximum separation of cohesive-contact property
ε_c^{ch}	Crushing strain of concrete
ε_t^{ck}	Tensile cracking strain of concrete
$A_{b,a}$	Local bearing area of the anchorage zone
$A_{s,s}$	Cross-sectional area of the shear zone
b	$\varepsilon_c^{pl}/\varepsilon_c^{in}$ ratio in Equation (6)
c_1 and c_2	Coefficients in Equation (7)
d	Stirrup diameter
d_c	Concrete compression-damage variable
d_s	Stud diameter in Equation (16)
d_t	Concrete tensile-damage variable
E_0	Undamaged elastic modulus of concrete
E_{cm}	Elastic modulus of concrete
E_s	Elastic modulus of steel
f_c	Concrete strength in Equations (16)–(18)
f_{cm}	Cylinder compressive strength of concrete

f_{tm}	Tensile strength of concrete
f_{u}	Ultimate tensile strength of steel
f_{y}	Yield strength of steel
G_{ch}	Crushing energy per unit area of concrete
G_{cm}	Shear modulus of concrete
G_{f}	Crushing energy per unit area of concrete
$h_{\text{b}}/h_{\text{s}}/h_{\text{a}}$	Height of the pressure-bearing zone/shear zone/anchorage zone
K	Second stress invariant ratio
$K_{0.2}$	Slip modulus (secant slope of the load-slip curves at a slip of 0.2 mm.)
$K_{0.2,\text{FE}}$	Slip modulus obtained from finite element
$K_{0.2,\text{pre}}$	Predicted slip modulus
$K_{0.2,\text{test}}$	Slip modulus obtained from test
K_{nn}, K_{ss}, K_{tt}	Elastic stiffness of cohesive contact property
k_s	Slip modulus of stud shear connector in Equation (16)
l_{ck}	Characteristic element length
Nomenclature	
P	Shear load
$P_{\text{b,a}}$	Compressive capacity of concrete in the anchorage zone
$P_{\text{b,b}}$	Compressive capacity of concrete in the pressure-bearing zone
$P_{\text{b,s}}$	Compressive capacity of concrete in the shear zone
$P_{\max}$	Ultimate shear resistance of stud shear connector in Equation (16)
P_{u}	Ultimate shear resistance
$P_{\text{u,FE}}$	Ultimate shear resistance obtained from finite element
$P_{\text{u,pre}}$	Predicted ultimate shear resistance
$P_{\text{u,test}}$	Ultimate shear resistance obtained from test
S	Relative ship
t_{n}, t_{s}, t_{t}	Tractions of the cohesive contact property
t_{s}, w_{s}	Thickness and width of the shear plate in the shear zone
$V_{\text{s,a}}$	Shear capacity of the anchorage zone
V_{ss}	Shear capacity of the shear zone
w	Cracking width of concrete
w_{c}	Cracking width corresponding to the zero tensile stress
$\alpha_{\text{c}}/\alpha_{\text{t}}/b_{\text{c}}/b_{\text{t}}$	Dimensionless coefficients in Equations (8)–(11)
α_{E}	Constant factor about concrete aggregates
ε	Flow potential eccentricity
ε_{c}	Compressive strain of concrete
ε_{tm}	Tensile peak strain of concrete
λ_{b}	Constant coefficient in Equation (14)
λ_{s}, α and β	Constant coefficient in Equation (13)
μ	Viscosity parameter
$\sigma_{\text{bo}}/\sigma_{\text{co}}$	Ratio of biaxial to uniaxial compressive strength
σ_{c}	Compressive stress of concrete
σ_{t}	Tensile stress of concrete
ψ	Dilatancy angle

References

1. Shim, C.-S.; Lee, P.-G.; Chang, S.-P. Design of shear connection in composite steel and concrete bridges with precast decks. *J. Constr. Steel Res.* **2001**, *57*, 203–219. [CrossRef]
2. Shim, C.S.; Kim, J.H.; Chang, S.P.; Chung, C.H. The behaviour of shear connections in a composite beam with a full-depth precast slab. *Struct. Build.* **2000**, *140*, 101–110. [CrossRef]
3. Song, S.-S.; Xu, F.; Chen, J.; Qin, F.; Huang, Y.; Yan, X. Feasibility and performance of novel tapered iron bolt shear connectors in demountable composite beams. *J. Build. Eng.* **2022**, *53*, 104528. [CrossRef]
4. Wang, H.; Liu, X.-G.; Yue, Q.-R.; Zheng, M.-Z. Shear resistance of a novel wet connection for prefabricated composite beams under shear-bending coupling loading. *J. Build. Eng.* **2021**, *45*, 103636. [CrossRef]

5. Johnson, R.P. *Composite Structures of Steel and Concrete: Beams, Slabs, Columns, and Frames for Buildings*, 3rd ed.; Blackwell Publishing: Hoboken, NJ, USA, 2008.
6. Wang, Y.-H.; Yu, J.; Liu, J.-P.; Chen, Y.F. Shear behavior of shear stud groups in precast concrete decks. *Eng. Struct.* **2019**, *187*, 73–84. [CrossRef]
7. Fang, Z.; Fang, H.; Huang, J.; Jiang, H.; Chen, G. Static behavior of grouped stud shear connectors in steel–precast UHPC composite structures containing thin full-depth slabs. *Eng. Struct.* **2022**, *252*, 113484. [CrossRef]
8. Ding, J.; Zhu, J.; Kang, J.; Wang, X. Experimental study on grouped stud shear connectors in precast steel- UHPC composite bridge. *Eng. Struct.* **2021**, *242*, 112479. [CrossRef]
9. Shim, C.-S.; Lee, P.-G.; Yoon, T.-Y. Static behavior of large stud shear connectors. *Eng. Struct.* **2004**, *26*, 1853–1860. [CrossRef]
10. Badie, S.S.; Tadros, M.K.; Kakish, H.F.; Splittgerber, D.L.; Baishya, M.C. Large Shear Studs for Composite Action in Steel Bridge Girders. *J. Bridg. Eng.* **2002**, *7*, 195–203. [CrossRef]
11. Wang, J.; Qi, J.; Tong, T.; Xu, Q.; Xiu, H. Static behavior of large stud shear connectors in steel-UHPC composite structures. *Eng. Struct.* **2018**, *178*, 534–542. [CrossRef]
12. Wang, J.; Xu, Q.; Yao, Y.; Qi, J.; Xiu, H. Static behavior of grouped large headed stud-UHPC shear connectors in composite structures. *Compos. Struct.* **2018**, *206*, 202–214. [CrossRef]
13. Pavlović, M.; Marković, Z.; Veljković, M.; Buđevac, D. Bolted shear connectors vs. headed studs behaviour in push-out tests. *J. Constr. Steel Res.* **2013**, *88*, 134–149. [CrossRef]
14. Tan, E.L.; Varsani, H.; Liao, F. Experimental study on demountable steel-concrete connectors subjected to combined shear and tension. *Eng. Struct.* **2019**, *183*, 110–123. [CrossRef]
15. Zhang, Y.; Chen, B.; Liu, A.; Pi, Y.-L.; Zhang, J.; Wang, Y.; Zhong, L. Experimental study on shear behavior of high strength bolt connection in prefabricated steel-concrete composite beam. *Compos. Part B Eng.* **2019**, *159*, 481–489. [CrossRef]
16. Fang, Z.; Fang, H.; Li, P.; Jiang, H.; Chen, G. Interfacial shear and flexural performances of steel–precast UHPC composite beams: Full-depth slabs with studs vs. demountable slabs with bolts. *Eng. Struct.* **2022**, *260*, 114230. [CrossRef]
17. Shariati, M.; Sulong, N.R.; Khanouki, M.A. Experimental assessment of channel shear connectors under monotonic and fully reversed cyclic loading in high strength concrete. *Mater. Des.* **2012**, *34*, 325–331. [CrossRef]
18. Baran, E.; Topkaya, C. Behavior of steel–concrete partially composite beams with channel type shear connectors. *J. Constr. Steel Res.* **2014**, *97*, 69–78. [CrossRef]
19. Shariati, M.; Sulong, N.R.; Shariati, A.; Kueh, A. Comparative performance of channel and angle shear connectors in high strength concrete composites: An experimental study. *Constr. Build. Mater.* **2016**, *120*, 382–392. [CrossRef]
20. Shariati, A.; Sulong, N.R.; Suhatril, M. Investigation of channel shear connectors for composite concrete and steel T-beam. *Int. J. Phys. Sci.* **2012**, *28*, 1828–1831. [CrossRef]
21. Shariati, M.; Sulong, N.R.; Suhatril, M.; Shariati, A.; Khanouki, M.A.; Sinaei, H. Behaviour of C-shaped angle shear connectors under monotonic and fully reversed cyclic loading: An experimental study. *Mater. Des.* **2012**, *41*, 67–73. [CrossRef]
22. Shariati, M.; Shariati, A.; Sulong, N.R.; Suhatril, M.; Khanouki, M.A. Fatigue energy dissipation and failure analysis of angle shear connectors embedded in high strength concrete. *Eng. Fail. Anal.* **2014**, *41*, 124–134. [CrossRef]
23. Qiu, S.-Y.; Guo, Y.-T.; Nie, X.; Fan, J.-S.; Tao, M.-X. Experimental study on shaped steel shear connectors used in large-scale composite structures. *J. Constr. Steel Res.* **2020**, *172*, 106201. [CrossRef]
24. Vianna, J.; Costa-Neves, L.; Vellasco, P.; de Andrade, S. Structural behaviour of T-Perfobond shear connectors in composite girders: An experimental approach. *Eng. Struct.* **2008**, *30*, 2381–2391. [CrossRef]
25. Zou, Y.; Qin, F.; Zhou, J.; Zheng, Z.; Huang, Z.; Zhang, Z. Shear behavior of a novel bearing-shear connector for prefabricated concrete decks. *Constr. Build. Mater.* **2020**, *268*, 121090. [CrossRef]
26. Guo, J.; Zhou, Z.; Zou, Y.; Zhang, Z.; Jiang, J.; Wang, X. Static behavior of novel shear connectors with post-poured UHPC for prefabricated composite bridge. *Structures* **2022**, *43*, 1114–1133. [CrossRef]
27. Cui, C.; Song, L.; Liu, R.; Liu, H.; Yu, Z.; Jiang, L. Shear behavior of stud connectors in steel bridge deck and ballastless track structural systems of high-speed railways. *Constr. Build. Mater.* **2022**, *341*, 127744. [CrossRef]
28. Wang, S.; Fang, Z.; Ma, Y.; Jiang, H.; Zhao, G. Parametric investigations on shear behavior of perforated transverse angle connectors in steel–concrete composite bridges. *Structures* **2022**, *38*, 416–434. [CrossRef]
29. Ataei, A.; Zeynalian, M. A study on structural performance of deconstructable bolted shear connectors in composite beams. *Structures* **2020**, *29*, 519–533. [CrossRef]
30. Lima, J.M.; Bezerra, L.M.; Bonilla, J.; Barbosa, W.C. Study of the behavior and resistance of right-angle truss shear connector for composite steel concrete beams. *Eng. Struct.* **2022**, *253*, 113778. [CrossRef]
31. *EN1992-1-4*; Design of Composite Steel and Concrete Structures. Part 1.1: General Rules and Rules for Buildings. European Committee for Standardization (CEN): Brussels, Belgium, 2004.
32. *GB 50017-2017*; Standard for Design of Steel Structures. China Architecture & Building Press: Beijing, China, 2017. (In Chinese)
33. *ABAQUS Software*, Version 6.14-5; Dassault Systèmes Simulia Corp: Providence, RI, USA, 2014. Available online: https://www.3ds.com/products-services/simulia/products/abaqus (accessed on 23 May 2023).
34. Nguyen, H.T.; Kim, S.E. Finite element modeling of push-out tests for large stud shear connectors. *J. Constr. Steel Res.* **2009**, *65*, 1909–1920. [CrossRef]

35. *ABAQUS, Theory Manual*, Version 6.14-5; Dassault Systèmes Simulia Corp: Providence, RI, USA, 2014. Available online: http://wufengyun.com:888/v6.14/books/usb/default.htm (accessed on 23 May 2023).
36. CEB-FIP. *Model Code 2010*; Thomas Telford: London, UK, 2010.
37. Birtel, V.; Mark, P. Parameterised finite element modelling of RC beam shear failure. In Proceedings of the 2006 ABAQUS Users' Conference, Providence, RI, USA, 16 November 2006. Available online: https://www.researchgate.net/publication/266411260_Parameterised_Finite_Element_Modelling_of_RC_Beam_Shear_Failure (accessed on 23 May 2023).
38. Alfarah, B.; López-Almansa, F.; Oller, S. New methodology for calculating damage variables evolution in Plastic Damage Model for RC structures. *Eng. Struct.* **2017**, *132*, 70–86. [CrossRef]
39. Hillenborg, A.; Modéer, M.; Petersson, P.E. Analysis of crack formation and crack growth in concrete by means of fracture mechanics and finite elements. In *Selected Landmark Papers in Concrete Materials*; American Concrete Institute: Farmington Hills, MI, USA, 2008. Available online: https://trid.trb.org/view/868768 (accessed on 23 May 2023).
40. Vonk, R.A. A micromechanical investigation of softening of concrete loaded in compression. *Heron* **1993**, *38*.
41. Hordijk, D.A. Tensile and tensile fatigue behaviour of concrete; experiments, modelling and analyses. *Heron* **1992**, *37*. Available online: https://trid.trb.org/view/366922 (accessed on 23 May 2023).
42. Zou, Y.; Di, J.; Zhou, J.; Zhang, Z.; Li, X.; Zhang, H.; Qin, F. Shear behavior of perfobond connectors in the steel-concrete joints of hybrid bridges. *J. Constr. Steel Res.* **2020**, *172*, 106217. [CrossRef]
43. Yu, J. *Study on Mechanical Behavior of Assembled Steel Concrete Composite Beams with Group Stud and Steel Block Connections*; Chongqing University: Chongqing, China, 2020. Available online: http://cdmd.cnki.com.cn/Article/CDMD-10611-1021541431.htm (accessed on 23 May 2023). (In Chinese)
44. Oehlers, D.; Coughlan, C. The shear stiffness of stud shear connections in composite beams. *J. Constr. Steel Res.* **1986**, *6*, 273–284. [CrossRef]
45. Suwaed, A.S.H.; Karavasilis, T.L. Novel Demountable Shear Connector for Accelerated Disassembly, Repair, or Replacement of Precast Steel-Concrete Composite Bridges. *J. Bridg. Eng.* **2017**, *22*, 04017052. [CrossRef]
46. Xu, H.; Zhang, S.; Rong, B. Investigation on shear behavior of studs and PBL shear connectors in steel-concrete hybrid bridge girder. *Structures* **2022**, *43*, 1422–1435. [CrossRef]
47. Langarudi, P.A.; Ebrahimnejad, M. Numerical study of the behavior of bolted shear connectors in composite slabs with steel deck. *Structures* **2020**, *26*, 501–515. [CrossRef]
48. Xu, X.; Liu, Y.; He, J. Study on mechanical behavior of rubber-sleeved studs for steel and concrete composite structures. *Constr. Build. Mater.* **2014**, *53*, 533–546. [CrossRef]
49. Zheng, S.; Liu, Y.; Yoda, T.; Lin, W. Parametric study on shear capacity of circular-hole and long-hole perfobond shear connector. *J. Constr. Steel Res.* **2016**, *117*, 64–80. [CrossRef]
50. Hu, Y.; Qiu, M.; Chen, L.; Zhong, R.; Wang, J. Experimental and analytical study of the shear strength and stiffness of studs embedded in high strength concrete. *Eng. Struct.* **2021**, *236*, 111792. [CrossRef]
51. *JTG/T D64-01-2015*; Specifications for Design and Construction of Highway Steel-concrete Composite Bridge. Ministry of Transport of the People's Republic of China, China Communications Publishing & Media Management Co., Ltd.: Beijing, China, 2015. (In Chinese)